

Gatemonium: A Voltage-Tunable Fluxonium

William M. Strickland, Bassel Heiba Elfeky, Lukas Baker, Andrea Maiani,

Jaewoo Lee, Ido Levy, Jacob Issokson, Andrei Vrajitoarea, and Javad Shabani

Center for Quantum Information Physics, Department of Physics, New York University, New York 10003, USA

(Dated: June 18, 2024)

We present a new fluxonium qubit design, gatemonium, based on an all superconductor-semiconductor hybrid platform exhibiting gate voltage tunability of E_J . We first show the principle of fluxonium operation in epitaxial Al/InAs heterostructure where the single Josephson junction can be controlled using gate voltage control, effectively tuning the weight of the fictitious phase particle through the ratio of the Josephson energy E_J to the charging energy E_C . The spectroscopy of the qubit shows tunability between plasmons to fluxons and their hybrid spectrum. We study two gatemonium devices with different charging energies and extract inductance of InAs-based Josephson junctions array. We also discuss future directions implementing a gate voltage tunable superinductance.

I. INTRODUCTION

Fluxonium qubits have become an incredibly promising alternative to the conventional transmon for quantum computation using superconducting circuits [1–3]. The fluxonium computational states have a suppressed transition matrix element when biased to near half a flux quantum, maximizing energy relaxation times [4–6]. First-order insensitivity to flux noise also exists at the magnetic “sweet spot”. Recently, coherence times exceeding 1 ms [7] and two-qubit gate fidelities exceeding 99.9% have been shown with fluxonium qubits [8, 9].

Fundamentally, the fluxonium qubit consists of a parallel Josephson junction, capacitor, and linear inductor. The associated energies are related to physical parameters in the circuit in the following way: the Josephson energy $E_J = \Phi_0 I_C / 2\pi$ for a junction critical current I_C , the charging energy $E_C = e^2 / 2C$ for a capacitance C , and the inductive energy $E_L = (\hbar / 2e)^2 / L$ for an inductance L . The magnetic flux quantum is $\Phi_0 = \hbar / 2e$ with Planck’s constant \hbar and the electron charge e . The linear inductance is typically implemented by a high kinetic inductance element, such as an array of Josephson junctions or a disordered superconductor [10]. The resulting energy spectrum, and relevant qubit properties such as frequency and anharmonicity, are uniquely defined by these relative energy scales. For example, circuits with small E_L lead to large phase fluctuations and the energy levels become flat with respect to external flux, suppressing flux noise dephasing. In contrast, circuits with large E_J / E_C have been shown to minimize the transition matrix element near half flux, leading to an enhanced energy relaxation time. These orthogonal use cases illustrate an important characteristic of fluxonium qubits that single mode devices can only protect from dephasing or bit flip errors at once. In analogy with the classical analogue of a mass in a corrugated potential, it is useful to think of fluxonium qubits in terms of their “weight”, where the “heavy” regime is where $E_J / E_C \gg 1$ and the “light” regime is where $E_J / E_C \sim 1$. Alternatively in the light

It may be beneficial in some cases to *in-situ* tune between the heavy and light regimes at will, requiring tunability of the energy scales. One such implementation could be realized by placing a split junction instead of the single junction, and a global magnetic field [4, 11] or a local flux lines, which will involve calibrating for cross terms in the mutual inductance matrix. Alternatively, gate-tunable semiconducting junctions could alleviate cross-talk due to electric field confinement. In addition, they also can be used to implement fast two qubit gates between fluxonia [6]. Earlier studies in InAs nanowire showed tunable E_J element in Ref. 12, however coherent manipulation of the qubit states was not performed.

In this report we introduce a fluxonium-style qubit with voltage-tunable E_J named “gatemonium”, referring to the gatemon qubit, being a gate voltage tunable transmon [13–17], shunted by a large inductance typical in fluxonium. The Josephson junctions in both in the single junction and, more notably, in the array are constructed from superconductor-semiconductor (super-semi) hybrid planar junctions. We exploit the *in-situ* E_J control to tune between the heavy and light fluxonium regimes. We utilize the tunable E_J to manipulate the energy spectrum at will, presented through one- and two-tone spectroscopy. We also report coherent manipulation of the plasmon mode observed by Rabi oscillations, as well as characterization of the T_1 energy relaxation.

II. SIMULATIONS

The fluxonium Hamiltonian is

$$\hat{H} = 4E_C \hat{n}^2 - E_J \cos\left(\hat{\phi} - 2\pi \frac{\Phi}{\Phi_0}\right) + \frac{E_L}{2} \left(\hat{\phi}\right)^2,$$

where the number of Cooper pairs \hat{n} and superconducting phase $\hat{\phi}$ form a pair of conjugated variables [18]. An external flux Φ applied through the loop tunes the relative depths of local minima. It is often useful to think of the system’s classical analog, being a particle with mass

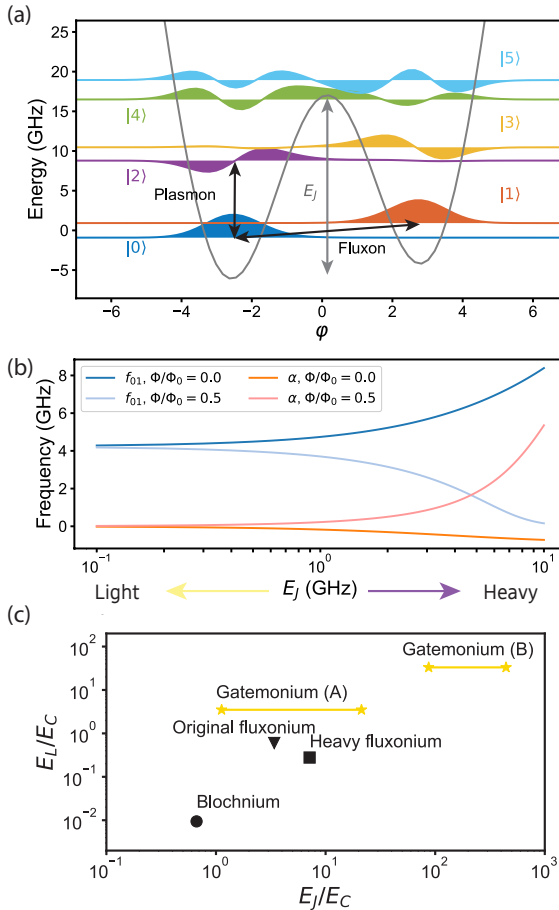


FIG. 1. E_J tuning in the gatemonium qubit: (a) Wavefunctions of the lowest levels in the gatemonium qubit in the heavy regime with $E_J = 17$ GHz, $E_L = 2.8$ GHz and $E_C = 0.8$ GHz. The external applied flux is $\Phi = 0.48\Phi_0$. (b) Qubit frequencies and anharmonicities at zero and half flux zero, and the anharmonicity α is maximized. As E_J decreases (light regime), the spectrum becomes harmonic, as the anharmonicity goes to zero, the qubit frequency becomes unchanged with flux, and the frequency approaches $\sqrt{8E_L E_C}$. (c) Landscape of fluxonium devices in terms of the relative capacitive, inductive and Josephson energies. The large E_J/E_C (heavy) regime where the transition matrix element is highly suppressed maximizes T_1 times. Two gatemonium qubits studied in this paper are also shown.

$1/8E_C$ and position φ sitting in the bottom of a parabolic potential corrugated by a cosine with amplitude E_J .

One example of the resulting wavefunctions in the phase basis is shown in Fig. 1(a) for $E_J/h = 12$ GHz, $E_L/h = 2.80$ GHz, and $E_C/h = 800$ MHz. The external flux Φ is set to $0.48\Phi_0$, close to the half flux degeneracy. The wavefunctions are offset on the y-axis based on their relative energies and labelled accordingly, with the ground state $|0\rangle$ (blue), the first excited state $|1\rangle$ (orange), and so on. The potential energy is shown (gray) with the barrier height between the lowest two wells being

Device	N_{JJ}	W_C (μm)	E_L (GHz)	E_C (MHz)
A	600	75	2.80	800
B	400	500	4.97	150

TABLE I. **Device parameters:** Devices A, and B with the number of Josephson junctions in the array N_{JJ} , the width of the capacitor W_C , the inductive energy E_L , and the charging energy E_C .

E_J . One can notice two distinct transitions corresponding to plasmon modes, with an energy $f_{02} = \sqrt{8E_J E_C}/h$, dictating transitions within each well, and fluxon modes, dictating transitions between different wells, with an energy of $f_{01} = 2\pi E_L/h$.

The Josephson potential localizes wavefunctions to individual wells, and the barrier height determines the suppression of the transition matrix element, influencing energy relaxation times T_1 inversely through Fermi's golden rule. Also interesting is to consider the susceptibility to flux noise through the derivative of the $|0\rangle$ to $|1\rangle$ transition frequency with respect to flux $df_{01}/d\Phi$. Alternatively, in the “light” regime, where $E_L \ll E_J, E_C$, the qubit is less sensitive to flux, and hence more protected from flux noise dephasing. This principle illustrates why it is advantageous to work at the half flux sweet spot, since the qubit is first-order insensitive to flux noise. A more detailed description of the error protection properties of fluxonium can be found in Ref 19.

Relevant to qubit operation, we plot the qubit f_{01} (blue) and anharmonicity α (red) as a function of E_J in Fig. 1(b) at zero (dark color) and half (light color) flux. The results are obtained for $E_L = 2.8$ GHz and $E_C = 800$ MHz. It can be seen that at large E_J , the qubit frequency at half flux approaches very low values, while the anharmonicity is very large and positive. As E_J approaches zero the qubit spectrum becomes harmonic, leading to a vanishing anharmonicity. In addition, the qubit becomes less flux tunable, and the frequency approaches a value set by $\sqrt{8E_L E_C}$.

To reiterate the importance of different fluxonium parameter regimes, we plot the landscape of different fluxonium energy regimes in Fig 1(c), adapted from Ref. 19. While it may be advantageous to be in the heavy regime for bit-flip protection and the light, so-called “Blochonium” regime [20] for phase flip protection, we show that with our gatemonium device we are able to tune the ratio of E_J/E_C by more than an order of magnitude connecting these two regimes.

III. DEVICE DESIGN AND FABRICATION

In this report we discuss two devices, A, and B. Their parameters are shown in Table 1. We show a false-color optical image of Device A in Fig. 2(a) with the capacitor in purple, the single junction in yellow, the array inductor in blue, the readout resonator in orange, and

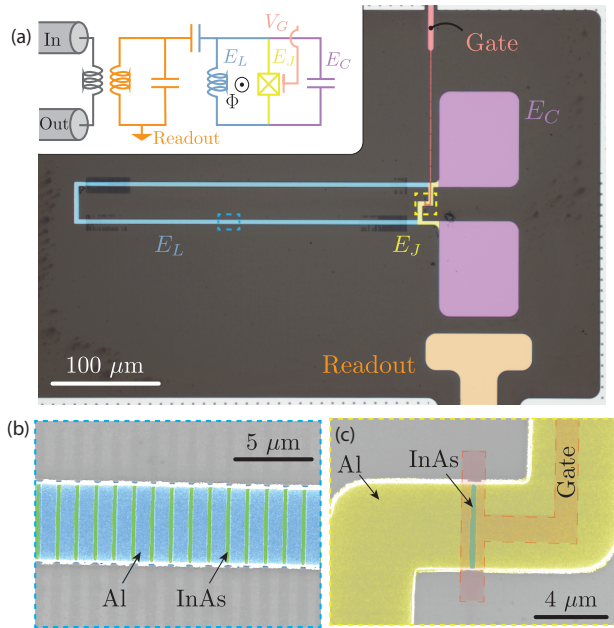


FIG. 2. Device optical image and circuit diagram: False-colored optical image of the gatemonium qubit is shown in (a) consisting of a shunt capacitor with charging energy E_C (purple), a planar Josephson junction with Josephson energy E_J (yellow), and a linear inductance, implemented in the form of a series of planar Josephson junctions with inductive energy E_L (blue). The inset shows an equivalent circuit diagram. Input and output transmission lines are inductively coupled to a readout resonator, which is capacitively coupled to the gatemonium. A zoomed in scanning electron micrograph (SEM) is shown in (b) of the Josephson junction array, with aluminum islands (blue) connected via Josephson coupling through InAs weak-links (green). A SEM image of the single junction before gate deposition is shown in (c) with aluminum leads (yellow) separated by an InAs weak link (green) and the top gate shaded placement (red).

the gate in red. The equivalent circuit diagram shown in the inset. The array is implemented in the form of 600 planar Josephson junctions in series, where a false-color scanning electron micrograph (SEM) of a nominally identical device is shown in Fig. 2(b). Al islands (blue) $1 \times 5 \mu\text{m}^2$ in size are connected through InAs weak links (green). A false color SEM of the single junction is shown in Fig. 1(c) before gate deposition, with Al leads in yellow and the InAs region in green. The top gate electrode used to tune E_J , shown schematically in red. The qubit is capacitively coupled to a readout resonator with a coupling strength of $g/2\pi = 150 \text{ MHz}$ as measured from the minimum detuning of the vacuum Rabi splitting [21]. The readout resonator is a $\lambda/4$ coplanar waveguide resonators and has internal quality factors of 5.5×10^3 measured at low power with the qubit far detuned, consistent with previous devices that underwent similar device fabrication [22]. The external quality factor was found to be 3.8×10^3 and the frequency was found to be $f_r = 7.4 \text{ GHz}$, leading to a coupling rate to the feedline of

$\kappa/2\pi = 1.8 \text{ MHz}$. Readout resonators are inductively coupled to a common feedline. We measure the complex transmission across the feedline S_{21} , as a function of probe frequency f_{probe} . Not pictured is an external charge line is coupled to the qubit capacitor. This line and the gate are both used to drive qubit transitions.

The device chip is mounted in a BeCu sample holder and shielded by aluminum and mu metal cans. Transmission lines on the chip are bonded to a printed circuit board using Al wirebonds. The package is mounted at the mixing chamber plate of a Oxford Instruments Triton, a cryogen-free dilution refrigerator, with a base temperature of 12 mK . Using a coil on the back of the sample holder we apply a global external magnetic flux through the loop Φ . A schematic of the wiring is shown in Appendix B.

IV. RESONATOR AND QUBIT SPECTROSCOPY

In this section we present qubit spectroscopy at different E_J values, representing the light, middle and heavy regimes. The Josephson energy increases with gate voltage nonmonotonically, which we describe in detail in Appendix C. First in the heavy regime, with $E_J = 12 \text{ GHz}$, we measure $|S_{21}|$ across the readout resonator for f_{probe} near the readout resonator frequency. We find that as a function of flux, the resonator is weakly tuned with flux. This is due mainly to the plasmon modes of the qubit, as we will see in two tone spectroscopy, dressing the resonator frequency due to dispersive coupling. Upon zooming in to $\Phi = \Phi_0/2$, one finds multiple avoided crossings of the resonator, being the qubit f_{01} and f_{02} modes, shown as orange and pink dashed lines respectively, for $E_J = 12.0 \text{ GHz}$, $E_L = 2.80 \text{ GHz}$ and $E_C = 800 \text{ MHz}$.

As the gate voltage decreases, E_J decreases to 4.0 GHz . The resonator now anticrosses with the f_{02} mode, shown in Fig. 3(b). The consistency of the fit with the data for different E_J values but fixed E_L and E_C verify that changes in the observed spectra are purely from the gate voltage changing E_J . We then tune to the light regime with $E_J = 0.9 \text{ GHz}$, where the resonator is now very weakly flux tunable, shown in Fig. 3(c).

The qubit response as a function of flux and gate voltage is directly measured through two-tone spectroscopy. We apply a drive tone of varying frequency f_{drive} and utilize dispersive readout to measure the qubit response. First in the heavy regime with $E_J = 17.5 \text{ GHz}$, at zero flux the qubit frequency is seen to be around 9.2 GHz and is tuned down to 8.7 GHz with flux, as shown in Fig. 3(d). At zero flux we know the lowest energy fluxonium mode should be a plasmon mode. Near $\Phi = 0.40\Phi_0$, one can see this mode then anticrosses with the fluxon mode, and the fluxon mode continues to disperse linearly with flux towards low frequency at $\Phi_0/2$. It should be noted that both the slope of this linearly dispersing fluxon mode, and the coupling between the fluxon and

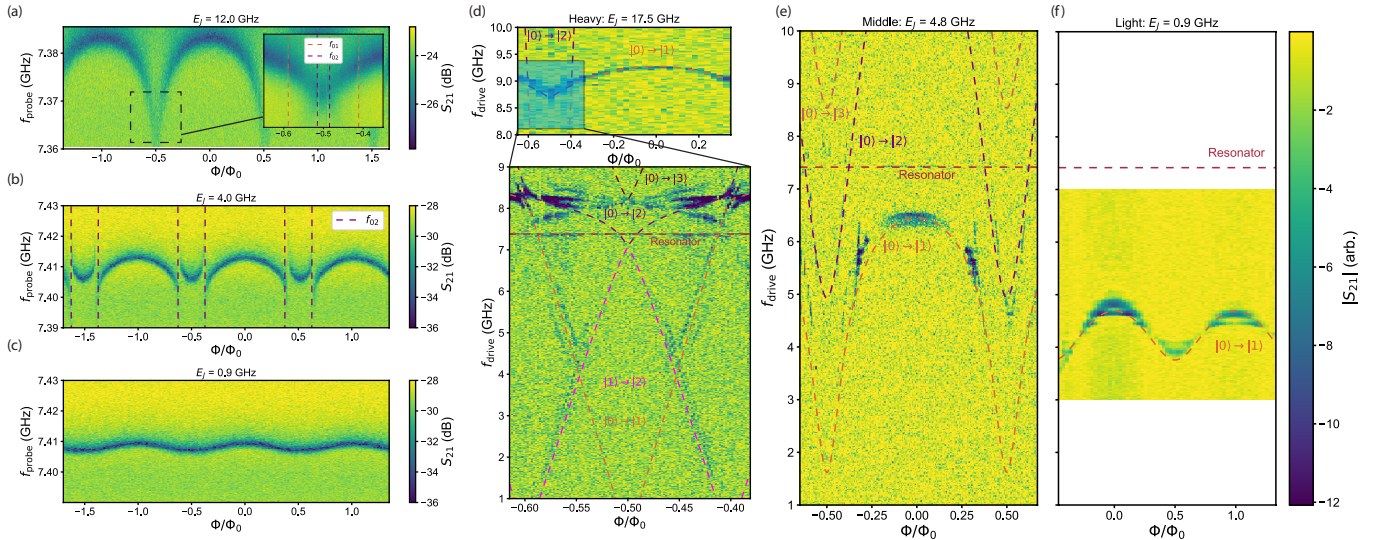


FIG. 3. One- and two-tone spectroscopy One-tone spectra are shown (a-c) of the transmission across a readout resonator $|S_{21}|$ as a function of applied external magnetic flux Φ/Φ_0 at different gate voltages. (a) The gatemonium is in the heavy regime with $E_J = 12.0$ GHz, and the dressed resonator frequency tunes periodically with flux due to coupling with the plasmon mode. Zooming in to the half flux (inset), one can see multiple crossings with the qubit f_{01} and f_{02} . (b) At $E_J = 4$ GHz, the fluxon and plasmon modes become hybridized and we see f_{02} cross with the readout resonator near half flux. (c) For $E_J = 0.9$ GHz the detuning of the fluxonium mode with the resonator increases, leading to a less pronounced flux dependence. Two-tone spectra are seen in (d-f). In the heavy regime $E_J = 17.5$ GHz the plasmon is weakly flux tunable and exhibits an avoided level crossing near half flux with the fluxon mode. Zooming in to near half flux one can observe the linearly dispersing fluxon mode, as well as the plasmon mode. (e) For $E_J = 4.8$ GHz the fluxon and plasmon modes are hybridized with f_{01} reaching 1.5 GHz at half flux and 6.2 GHz at zero flux. (f) As E_J decreases, the gatemonium spectrum becomes harmonic and weakly flux tunable, where f_{01} is sinusoidal with flux and centered around a value of $\sqrt{8E_L E_C}$.

the plasmon mode depends on the ratio of E_J/E_L . The qubit frequency at half flux in this regime reaches as low as $f_{01} = 75$ MHz inferred from the fit.

We then tune to the middle regime, with $E_J = 4.8$ GHz in Fig. 3(e). One can notice that now the plasmon mode at zero flux is at 6.2 GHz, and tunes down to 1.5 GHz with flux. The $|0\rangle$ to $|2\rangle$ transition can be seen to cross with the readout resonator at 7.4 GHz, which yields a one tone response similar to what was observed in Fig. 1(b). The plasmon and the fluxon modes in the middle regime are much more strongly coupled as compared to those in the heavy regime. E_J is then decreased to 0.9 GHz, where the qubit response to flux is nearly sinusoidal, centered around a frequency of 4.23 GHz. Here the frequency is entirely dominated by E_L and E_C for very small E_J , and the spectrum is purely harmonic with a lowest transition frequency equal to $\sqrt{8E_L E_C}$.

V. PLASMON TIME DOMAIN CHARACTERIZATION

We employ homodyne detection of the qubit state in a variety of pulsed measurements on Device B. The qubit gate voltage is such that we are in the heavy regime with $E_J = 30$ GHz. Looking at the spectrum near zero flux, the lowest energy transition corresponds to a plasmon

transition. E_J at this point is 6.5 GHz.

We apply a short square pulse near the qubit frequency with a width of τ_{Rabi} while applying a weak continuous readout. We find that as a function of the pulse width, the homodyne detection voltage V_H oscillates, corresponding to Rabi oscillations. We see the Rabi frequency change as a function of drive detuning from the qubit frequency, being 6.5 GHz in Fig. 4(a). The inset shows a linecut fit to a decaying sinusoid, revealing the coherence time associated with the Rabi manipulation, being about 66 ns. We also find the Rabi frequency decrease as we decrease the drive power as shown in Fig. 4(b). We use this measurement to calibrate the width of a π pulse, which drive the qubit from the $|0\rangle$ to the $|1\rangle$ state. We then perform a T_1 measurement and find a $T_1 = 90$ ns. This is consistent with gatemon T_1 times measured on using a similar fabrication procedure [17].

We note that in Device B we could not couple to the fluxon modes due to the much smaller E_C . It could be possible to utilize a Raman driving procedure as used in Ref. 5 to couple to the fluxon modes in the heavy regime. We hope to measure the coherence properties of the fluxon modes in the gatemonium qubit in a future experiment. In the future it would be worthwhile to investigate the effect of quasiparticle and phase slip processes of gatemonium dephasing [23] as well as gate-tuning the Josephson junction array as well.

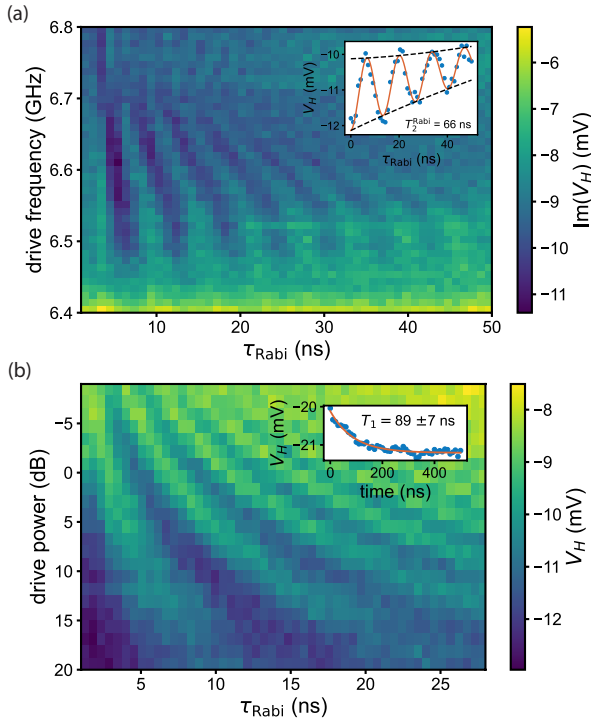


FIG. 4. Time domain Measurement in Plasmon Regime: Rabi oscillations as a function of drive frequency and drive power are shown in (a) and (b) respectively. A fit to the decaying sinusoid is shown in the inset yielding $T_2^{\text{Rabi}} = 70$ ns. E_J is 6.5 GHz.

VI. CONCLUSION

We present an introduction to the gatemonium qubit, along with a detailed analysis of the qubit spectra at different E_J regimes as a function of flux. The qubit E_J is tunable over an order of magnitude, accessing the light and heavy fluxonium regimes. The inductor was achieved using 600 super-semi Josephson junctions in series for a 1 μ H inductance. We find the array of superconductor-semiconductor junctions can be treated as a linear inductor through a good fit to the data. We measured coherence times from Rabi oscillations and a T_1 measurement of the plasmon mode in the heavy regime and found it corresponds very closely to what has been observed in the past for gatemon qubits on this platform.

We believe this is an exciting first step to making fluxonium-style qubits on this material platform. There has been increased interest in using different types of junction array materials which can lead to higher Josephson plasma frequencies, possibly for higher operating temperatures and for achieving larger inductances. While the junction leads in conventional superconductor-insulator-superconductor junctions effectively form a parallel plate capacitor, the junction leads in a superconductor junction form a coplanar capacitor, yielding a reduced Josephson capacitance C_J and increases

the Josephson plasma frequency $\omega_p = 1/\sqrt{L_J C_J}$ for L_J the Josephson inductance. Since the maximum operating frequency of the array is enhanced, one can imagine operating qubits at higher temperatures based on these materials. In addition, the number of Josephson junctions in the array can be enhanced, since the maximum number of junctions in the array is bounded from above by the square root of the ratio of C_J to the capacitance of each island to ground C_G , where both are on the order of 1 fF, as opposed to conventional superconductor-insulator-superconductor junctions, which commonly have C_J more than 10 fF. In addition, the semiconductor weak-links in the array can possibly give rise to a voltage tunable superinductance [24]. For these reasons, a Josephson junction array based on superconductor-semiconductor hybrid materials may be useful for superconducting qubits, amplifiers [25], couplers [26–29] and metamaterials [30] in the future.

VII. ACKNOWLEDGEMENTS

We thank Andrew Higginbottham, Shayam Shankar, Archana Kamal, Maxim Vavilov, Vlad Manucharyan, Srivatsan Chakram, Peter Schüffelgen, and Charlie Tahan for fruitful conversations. We acknowledge support from the Army Research Office agreement W911NF2110303. W.M.S. acknowledges funding from the ARO/LPS QuaCR Graduate Fellowship. The authors acknowledge MIT Lincoln Laboratory and IARPA for providing the TWPA used in this work. We also acknowledge MIT LL SQUIL Foundry for providing qubits that provided insight for calibration of the fridge thermalization steps.

APPENDIX A: MATERIALS GROWTH AND FABRICATION

The device is based on an InAs 2DEG grown by molecular beam epitaxy capped with an aluminum layer *in situ*. Details of the growth procedure can be found in Refs. 31–33. The structure is grown on a semi-insulating, Fe-doped, 500 μ m thick, 2-inch diameter, single-side polished InP wafer (AXT Inc.). The oxide is thermally desorbed under an arsenic overpressure in an ultrahigh vacuum chamber. A superlattice and graded buffer layer are grown in order to minimize compressive strain on the active region. The quantum well is formed by a 4 nm bottom $\text{In}_{0.81}\text{Ga}_{0.19}\text{As}$ barrier, a 4 nm InAs layer, and a 10 nm $\text{In}_{0.81}\text{Ga}_{0.19}\text{As}$ top barrier. The wafer is delta-doped with Si 6 nm below the active region. The wafer is then cooled to below 0 $^{\circ}\text{C}$ for the deposition of a 30 nm thick Al layer, measured by atomic force microscopy.

The device is fabricated using standard electron beam lithography using polymethyl methacrylate resist. There are three lithography layers. We first dice a 7×7 mm² piece of the wafer and clean successively in dioxolane and

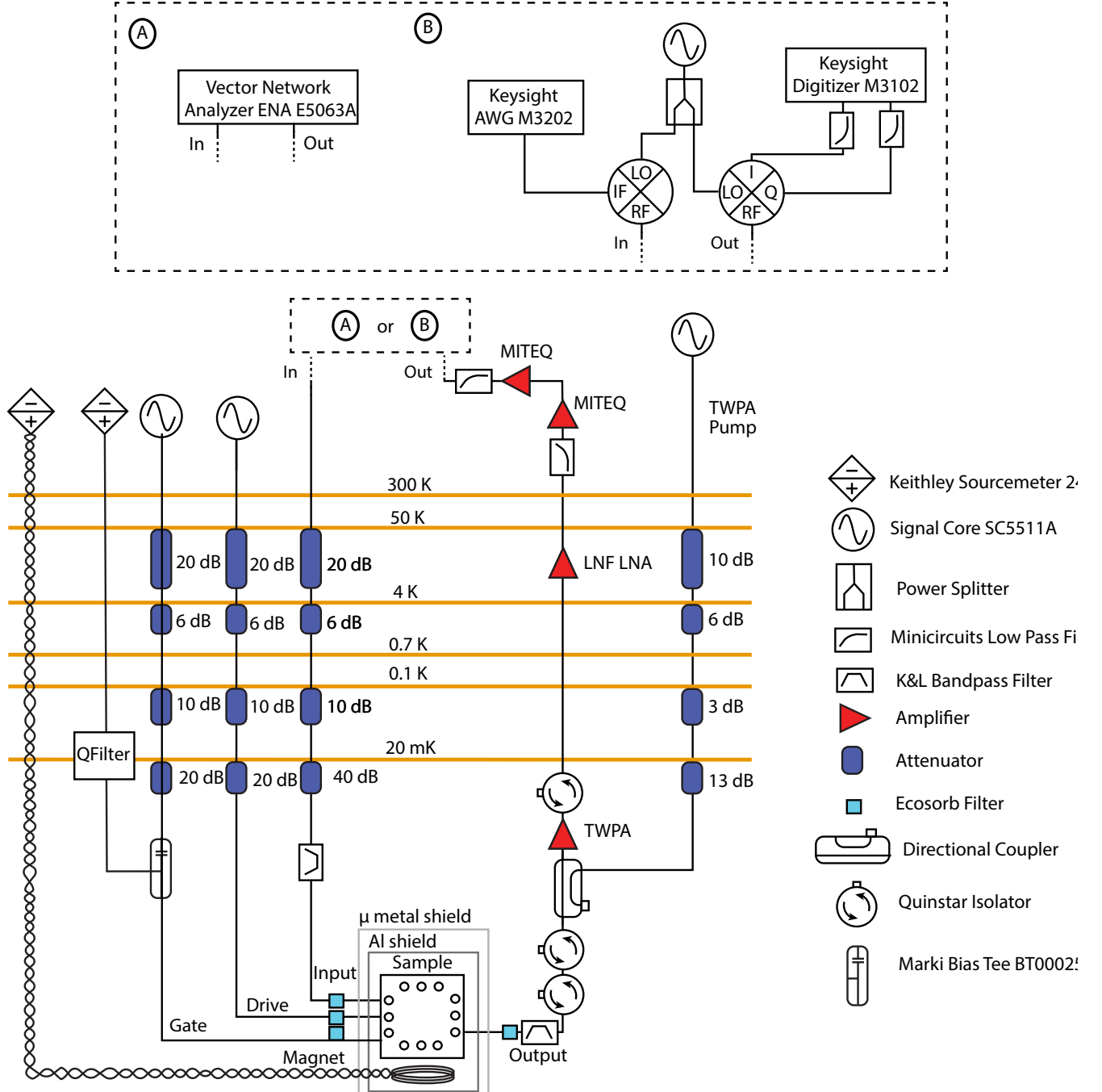


FIG. 5. Dilution refrigerator wiring diagram

isopropyl alcohol. We then define the microwave circuit and perform a wet chemical etch of the Al and III-V layers using Transene Type D and a solution of phosphoric acid, hydrogen peroxide, and deionized water in a volume

metric ratio of 1:1:40 respectively. We then define the Josephson junction by etching a narrow strip in the aluminum layer, defining two superconducting leads of the Josephson junction separated by 100 nm. We deposit a

40 nm thick layer of AlO_x at 40 °C by atomic layer deposition, followed by a 100 nm thick layer of Al to serve as the top gate to control E_J . The top gate is defined in a liftoff step after a sputter deposition of 100 nm of Al.

APPENDIX B: WIRING

The chip is mounted on thin copper sample holders and placed in a printed circuit board (PCB). Transmission lines on the chip are connected to waveguides on the PCB by aluminum wirebonds. A gold plated Be/Cu cavity with resonances above 10 GHz encloses the chip, and an Al shield encloses the sample. Magnetic field is provided by a coil within the Al shield.

The sample is mounted on a cold finger attached to the mixing chamber plate of a cryogen-free dilution refrigerator with a base temperature of 15 mK. Input and output lines are connected by copper coaxial cables with SMA connectors. The input rf signal across the common feedline is attenuated by -76 dB from room temperature to base temperature. Drive signals are attenuated by -56 dB. At the mixing chamber plate, the incoming rf signal passes through an Eccosorb filter and a K&L filter with a DC to 12 GHz pass band. The outgoing signal is passed through another eccosorb filter and K&L filter, then to two isolators and a directional coupler before being amplified by a travelling wave parametric amplifier. The tone used to pump the amplifier is attenuated by -39 dB. The signal is then further amplified by a low noise amplifier at 4 K, and then amplified and filtered at room temperature. DC signals are supplied by a voltage source at room temperature and low pass filtered at the mixing chamber plate. DC and RF are combined by bias tees at base temperature.

We use a vector network analyzer in order to measure one and tone spectroscopy data. Signal generators are used to supply a continuous wave signal to drive the qubit for both two tone spectroscopy and for time domain measurements. For time domain measurements, readout and drive continuous wave signals are mixed with the output of an arbitrary waveform generator (AWG) using double balanced mixers. The AWG has a sampling rate of 1 GSa/s. The readout signal is split by a power divider and supplied to the local oscillator port of an IQ mixer, and the outgoing, amplified signal is sent to the RF port, where I and Q quadratures are then recorded using a digitizer with a sampling rate of 500 MSa/s. A schematic of the wiring is shown in Fig. 6.

APPENDIX C: GATE VOLTAGE TUNING OF THE JOSEPHSON ENERGY

The Fermi level in an InAs layer is biased by a gate voltage, tuning the occupation of current carrying Andreev bound states [34]. The inductance and qubit frequency are then sensitive to applied gate voltage: for de-

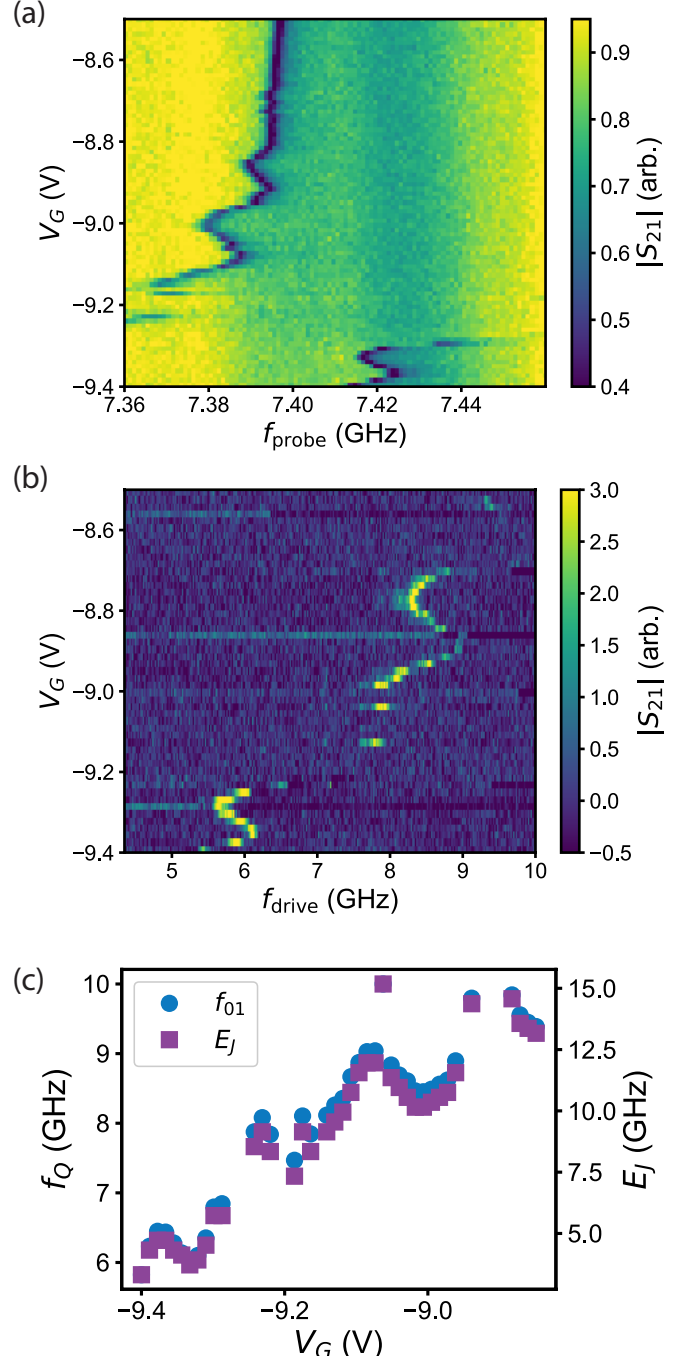


FIG. 6. **Gate voltage tuning of E_J :** (a) The top gate voltage V_G tunes the critical current in the Josephson junction, forcing the qubit mode to undergo an avoided level crossing with the readout resonator. (b) Two tone spectroscopy reveals the qubit f_{01} mode as a function of gate voltage. (c) We extract f_{01} as a function of gate voltage from the data, and compare this to simulations of the expected E_J for a given f_{01} to map these values to E_J .

creasing gate voltage, the critical current decreases, the inductance increases, and the qubit frequency decreases.

We show single and two tone spectroscopy as a function of gate voltage in Fig. 5. We see that as the gate voltage is tuned to negative values, the resonator exhibits an avoided level crossing with the qubit. The minimum detuning of these two modes yields twice the coupling strength.

In the same gate voltage range we conduct two tone spectroscopy. We find that for a junction near depletion the qubit undergoes mesoscopic conductance fluctuations, leading to a nonmonotonic behavior with gate voltage [35, 36]. The plasmon frequency as a function of

gate voltage is seen to tune between 9.5 GHz and 5 GHz from -8.5 to -9.4 V. Extracting the qubit frequency from the two tone data allows us to determine E_J as a function of gate voltage. At zero flux, we are able to calculate the expected f_{01} and match this with our measured data in order to map the measured qubit frequency to an E_J value. We note that due to the coupling of the plasmon and fluxon modes, this does not follow the conventional plasmon frequency $\sqrt{8E_JE_C}$.

[1] V. E. Manucharyan, J. Koch, L. I. Glazman, and M. H. Devoret, *Science* **326**, 113 (2009).

[2] A. Blais, R.-S. Huang, A. Wallraff, S. M. Girvin, and R. J. Schoelkopf, *Phys. Rev. A* **69**, 062320 (2004).

[3] J. Koch, T. M. Yu, J. Gambetta, A. A. Houck, D. I. Schuster, J. Majer, A. Blais, M. H. Devoret, S. M. Girvin, and R. J. Schoelkopf, *Phys. Rev. A* **76**, 042319 (2007).

[4] Y.-H. Lin, L. B. Nguyen, N. Grabon, J. San Miguel, N. Pankratova, and V. E. Manucharyan, *Phys. Rev. Lett.* **120**, 150503 (2018).

[5] N. Earnest, S. Chakram, Y. Lu, N. Irons, R. K. Naik, N. Leung, L. Ocola, D. A. Czaplewski, B. Baker, J. Lawrence, J. Koch, and D. I. Schuster, *Phys. Rev. Lett.* **120**, 150504 (2018).

[6] H. Zhang, S. Chakram, T. Roy, N. Earnest, Y. Lu, Z. Huang, D. K. Weiss, J. Koch, and D. I. Schuster, *Phys. Rev. X* **11**, 011010 (2021).

[7] A. Somoroff, Q. Ficheux, R. A. Mencia, H. Xiong, R. Kuzmin, and V. E. Manucharyan, *Phys. Rev. Lett.* **130**, 267001 (2023).

[8] L. Ding, M. Hays, Y. Sung, B. Kannan, J. An, A. Di Paolo, A. H. Karamlou, T. M. Hazard, K. Azar, D. K. Kim, B. M. Niedzielski, A. Melville, M. E. Schwartz, J. L. Yoder, T. P. Orlando, S. Gustavsson, J. A. Grover, K. Serniak, and W. D. Oliver, *Phys. Rev. X* **13**, 031035 (2023).

[9] F. Bao, H. Deng, D. Ding, R. Gao, X. Gao, C. Huang, X. Jiang, H.-S. Ku, Z. Li, X. Ma, X. Ni, J. Qin, Z. Song, H. Sun, C. Tang, T. Wang, F. Wu, T. Xia, W. Yu, F. Zhang, G. Zhang, X. Zhang, J. Zhou, X. Zhu, Y. Shi, J. Chen, H.-H. Zhao, and C. Deng, *Phys. Rev. Lett.* **129**, 010502 (2022).

[10] T. M. Hazard, A. J. Kerman, K. Serniak, and C. Tahan, Superconducting-semiconducting voltage-tunable qubits in the third dimension (2022).

[11] M. Specker, P. Paluch, N. Gosling, N. Drucker, S. Matityahu, D. Gusenkova, S. Günzler, D. Rieger, I. Takmakov, F. Valenti, P. Winkel, R. Gebauer, O. Sander, G. Catelani, A. Shnirman, A. V. Ustinov, W. Wernsdorfer, Y. Cohen, and I. M. Pop, *Nature Physics* **19**, 1320 (2023).

[12] M. Pita-Vidal, A. Bargerbos, C.-K. Yang, D. J. van Woerkom, W. Pfaff, N. Haider, P. Krogstrup, L. P. Kouwenhoven, G. de Lange, and A. Kou, *Phys. Rev. Appl.* **14**, 064038 (2020).

[13] G. de Lange, B. van Heck, A. Bruno, D. J. van Woerkom, A. Geresdi, S. R. Plissard, E. P. A. M. Bakkers, A. R. Akhmerov, and L. DiCarlo, *Phys. Rev. Lett.* **115**, 127002 (2015).

[14] T. W. Larsen, K. D. Petersson, F. Kuemmeth, T. S. Jespersen, P. Krogstrup, J. Nygård, and C. M. Marcus, *Phys. Rev. Lett.* **115**, 127001 (2015).

[15] L. Casparis, M. R. Connolly, M. Kjaergaard, N. J. Pearson, A. Kringhøj, T. W. Larsen, F. Kuemmeth, T. Wang, C. Thomas, S. Gronin, G. C. Gardner, M. J. Manfra, C. M. Marcus, and K. D. Petersson, *Nature Nanotechnology* **13**, 915 (2018).

[16] J. O'Connell Yuan, K. S. Wickramasinghe, W. M. Strickland, M. C. Dartailh, K. Sardashti, M. Hatefipour, and J. Shabani, *Journal of Vacuum Science & Technology A* **39**, 033407 (2021).

[17] W. M. Strickland, L. J. Baker, J. Lee, K. Dindial, B. H. Elfeky, P. J. Strohbeen, M. Hatefipour, P. Yu, I. Levy, J. Issokson, V. E. Manucharyan, and J. Shabani, *Phys. Rev. Res.* **6**, 023094 (2024).

[18] A. Blais, A. L. Grimsmo, S. M. Girvin, and A. Wallraff, *Rev. Mod. Phys.* **93**, 025005 (2021).

[19] A. Gynis, A. Di Paolo, J. Koch, A. Blais, A. A. Houck, and D. I. Schuster, *PRX Quantum* **2**, 030101 (2021).

[20] I. V. Pechenezhskiy, R. A. Mencia, L. B. Nguyen, Y.-H. Lin, and V. E. Manucharyan, *Nature* **585**, 368 (2020).

[21] A. Wallraff, D. I. Schuster, A. Blais, L. Frunzio, R.-S. Huang, J. Majer, S. Kumar, S. M. Girvin, and R. J. Schoelkopf, *Nature* **431**, 162 (2004).

[22] W. M. Strickland, B. H. Elfeky, J. O. Yuan, W. F. Schiela, P. Yu, D. Langone, M. G. Vavilov, V. E. Manucharyan, and J. Shabani, *Physical Review Applied* **19**, 034021 (2023).

[23] B. H. Elfeky, W. M. Strickland, J. Lee, J. T. Farmer, S. Shanto, A. Zarassi, D. Langone, M. G. Vavilov, E. M. Levenson-Falk, and J. Shabani, Quasiparticle dynamics in epitaxial al-inas planar josephson junctions (2023), arXiv:2303.04784 [cond-mat.mes-hall].

[24] M. T. Bell, I. A. Sadovskyy, L. B. Ioffe, A. Y. Kitaev, and M. E. Gershenson, *Phys. Rev. Lett.* **109**, 137003 (2012).

[25] D. Phan, P. Falthansl-Scheinecker, U. Mishra, W. M. Strickland, D. Langone, J. Shabani, and A. P. Higginbotham, Semiconductor quantum-limited amplifier (2022).

[26] K. Sardashti, M. C. Dartailh, J. Yuan, S. Hart, P. Gumann, and J. Shabani, *IEEE Transactions on Quantum Engineering* **1**, 1 (2020).

[27] N. Materise, M. C. Dartailh, W. M. Strickland, J. Shabani, and E. Kapit, *Quantum Science and Technology* **8**,

045014 (2023).

[28] Z. Qi, H. Xie, J. Shabani, V. E. Manucharyan, A. Levchenko, and M. G. Vavilov, Phys. Rev. B **97**, 134518 (2018).

[29] L. Casparis, N. J. Pearson, A. Kringsøj, T. W. Larsen, F. Kuemmeth, J. Nygård, P. Krogstrup, K. D. Petersson, and C. M. Marcus, Phys. Rev. B **99**, 085434 (2019).

[30] L. J. Splitthoff, M. C. Belo, G. Jin, Y. Li, E. Greplova, and C. K. Andersen, Gate-tunable phase transition in a bosonic su-schrieffer-heeger chain (2024), arXiv:2404.07371 [quant-ph].

[31] J. Shabani, M. Kjaergaard, H. J. Suominen, Y. Kim, F. Nichele, K. Pakrouski, T. Stankevic, R. M. Lutchyn, P. Krogstrup, R. Feidenhans'l, S. Kraemer, C. Nayak, M. Troyer, C. M. Marcus, and C. J. Palmstrøm, Phys. Rev. B **93**, 155402 (2016).

[32] K. S. Wickramasinghe, W. Mayer, J. Yuan, T. Nguyen, L. Jiao, V. Manucharyan, and J. Shabani, Applied Physics Letters **113**, 262104 (2018).

[33] W. M. Strickland, M. Hateipour, D. Langone, S. M. Farzaneh, and J. Shabani, Applied Physics Letters **121**, 092104 (2022), <https://doi.org/10.1063/5.0101579>.

[34] C. W. J. Beenakker, Phys. Rev. B **46**, 12841 (1992).

[35] A. Kringsøj, L. Casparis, M. Hell, T. W. Larsen, F. Kuemmeth, M. Leijnse, K. Flensberg, P. Krogstrup, J. Nygård, K. D. Petersson, and C. M. Marcus, Phys. Rev. B **97**, 060508 (2018).

[36] A. Danilenko, D. Sabonis, G. W. Winkler, O. Erlandsen, P. Krogstrup, and C. M. Marcus, Few-mode to mesoscopic junctions in gatemon qubits (2022).